Supporting Information for

Antioxidative, low-concentration MXene inks with high-viscosity for

infrared encryption and thermal energy harvesting

Xueting Zhang, Ruiqi Yu, Mengyao Wang, Zifan Song, Xiangxin Li, Yadong Gao,

Wanjie Wang* and Jianfeng Wang*

School of Materials Science and Engineering, Zhengzhou University, Zhengzhou

450001, China

**Corresponding Author: E-mail: wwj@zzu.edu.cn; jfw@zzu.edu.cn；

This supplementary file includes:

Supplementary Notes S1 to S3

Figures S1 to S26

Table S1 to S2

References

Other supplementary materials for this manuscript include the following:

Videos S1 to S8

Supplementary Notes S1: Calculation of average mid-IR spectral emissivity

The average mid-IR spectral emissivity at 7~14 μm of films was calculated according to the following equations (1):[1]

$$\bar{\varepsilon} = \frac{\int_{7\mu m}^{14\mu m} \varepsilon(\lambda)E(\lambda,T)d\lambda}{\int_{7\mu m}^{14\mu m} E(\lambda,T)d\lambda} \tag{1}$$

where $\varepsilon(\lambda)$ is the spectral emissivity measured based on the thermal radiation relation, ie, $\varepsilon = 1 - r - \tau$ (ε, r and τ are emissivity, reflectivity, and transmissivity, respectively). $E(\lambda,T)$ represents spectral radiance emitted from blackbody (300 K) and $\varepsilon(\lambda)$ represents ε at wavelength λ measured at room temperature (298 K).

Supplementary Notes S2: Calculation of infrared emissivity by the radiative compensation method

Here, the radiative compensation method was employed to obtain the IR emissivity, which adjusts the emissivity in an IR camera to modify the radiant temperature of an object. The Stefan-Boltzmann formula (2):

$$P = \varepsilon\delta T^4 \tag{2}$$

where δ represents the Stefan-Boltzmann constant, elucidates that the thermal radiation emitted by an object is intricately dependent on the square of the surface infrared emissivity (ε) and the surface thermodynamic temperature (T). When the radiant temperature matches the surface temperature measured by a thermocouple, the IR emissivity in the IR camera represents the emissivity of the target.[2]

Supplementary Notes S3: Calculation of average solar spectral absorptivity

The average spectral absorptivity (α) at 400-780 nm of different films is the irradiance-weighted average of its spectral absorptivity and is calculated according to the following equation (3):[3]

$$\bar{\alpha} = \frac{\int_{400nm}^{760nm} \alpha(\lambda)i(\lambda)d\lambda}{\int_{400nm}^{760nm} i(\lambda)d\lambda} \tag{3}$$

where $\alpha(\lambda)$ is spectral absorptivity obtained based on the relation, *i.e.,* $\alpha = 1 - r - T$ (α, r and T are spectral absorptivity, reflectivity, and transmissivity, respectively). $\alpha(\lambda)$ represents absorptivity at wavelength λ measured at room temperature (298 K) and $i(\lambda)$ represents spectral solar power (AM 1.5G).
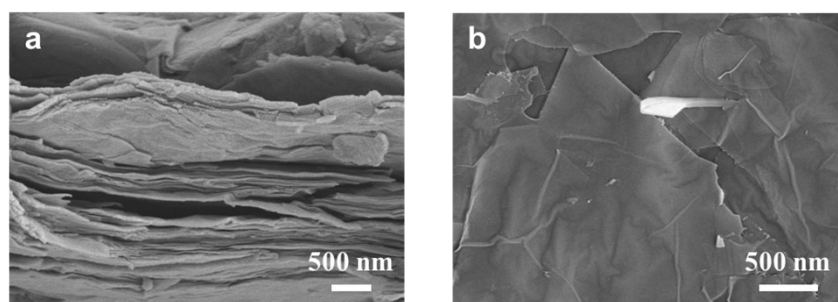
Figure S1. Scanning electron microscope (SEM) image of (a) fracture surface of MXene film and (b) surface of MXene nanosheet.
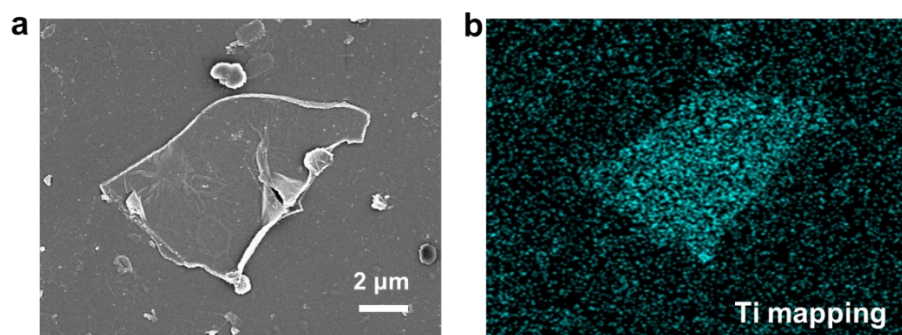

Figure S2. SEM image of MXene/GA nanosheets (a) and corresponding elemental mapping of Ti (b).
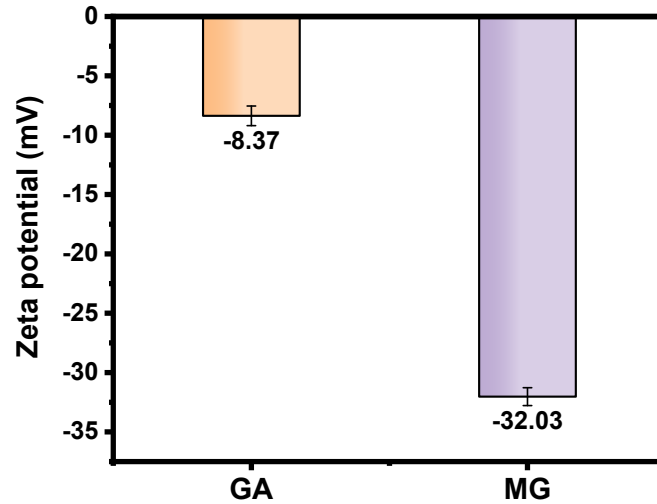
Figure S3. Zeta potential values of GA and MG. The surface of MXene nanosheets is negatively charged and the edge is positively charged,[4-6] while GA is electronegative in solution. Therefore, under electrostatic interaction, GA is more dispersed around the MXene layer in the form of wrapped nanosheets. On the other hand, under the balanced action of repulsive force, the dispersion of MG nanosheets presents a stable suspension state.
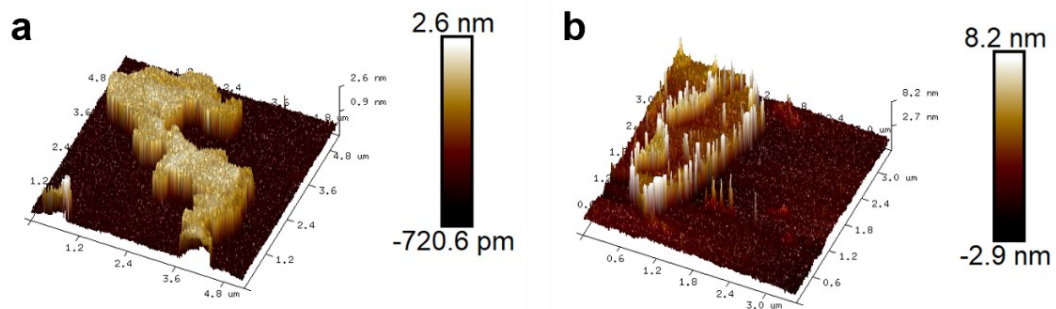

Figure S4. 3D images of (a) MXene and (b) MG nanosheets obtained from atomic force microscopy (AFM).
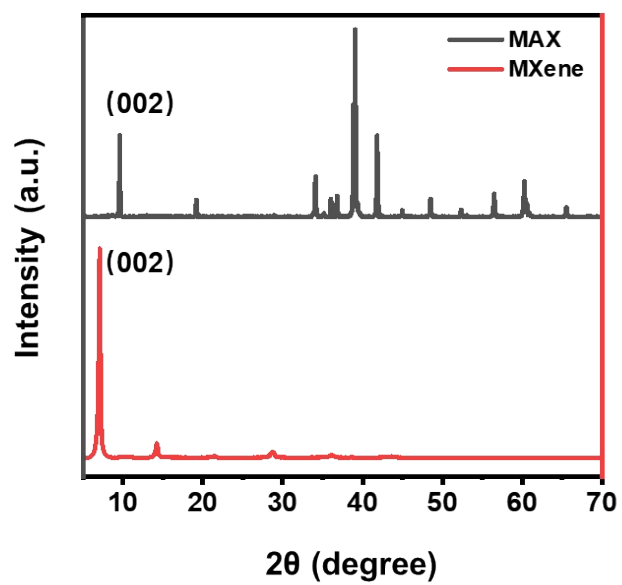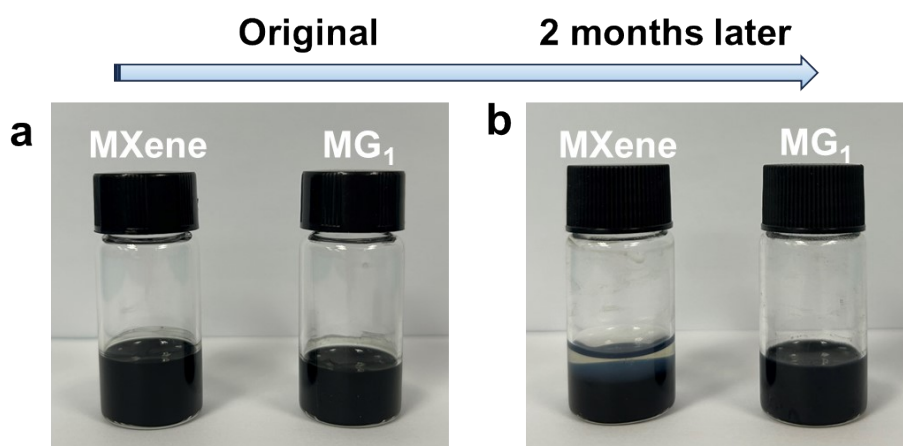
Figure S5. XRD patterns of MAX and MXene.

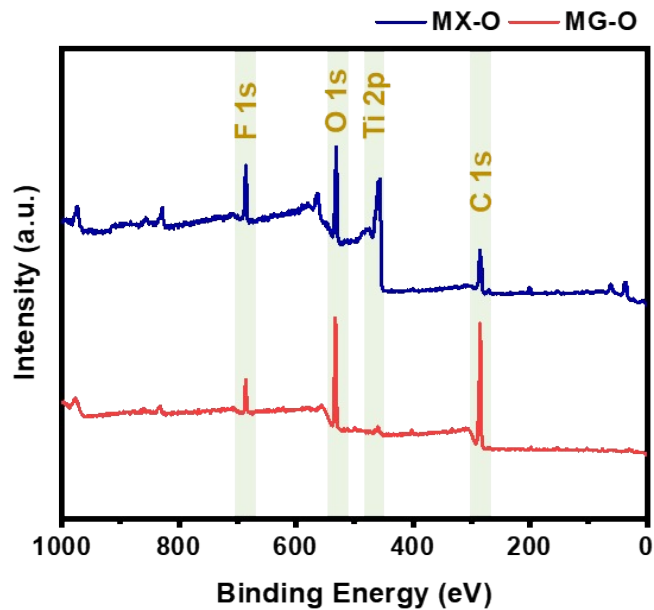**Figure S6**. Digital images of (a) original and (b) aged MXene or MG_1 ink.

Figure S7. The XPS survey spectra of MXene and MG stored for two months (named as MX-O, MG-O, respectively), labeled with characteristic peaks of Ti 2p, C 1s, O 1s, and F 1s. The XPS spectra of MX-O and MG-O, highlight characteristic peaks of Ti 2p, C 1s, O 1s, and F 1s in MX-O, while characteristic peak of Ti 2p is very weak in MG-O compared with that in MX-O.
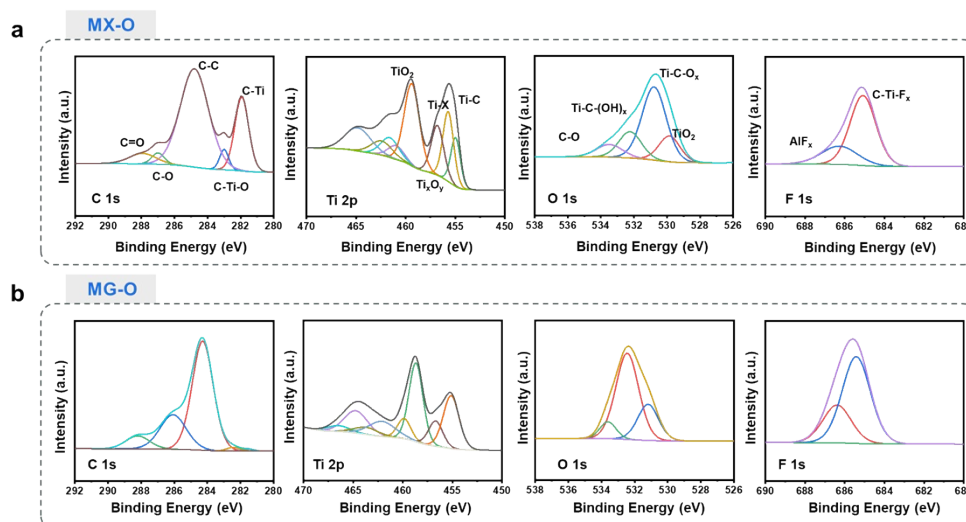
Figure S8. Component peak fittings of XPS spectra for (a) MXene after oxidation (MX-O) and (b) MG after oxidation (MG-O). In the XPS C 1s spectrum, all peaks attributed to MXene were observed in both MXene and MG samples, suggesting that the structure of the MXene nanosheets remained intact following the mixing process. However, the increase in C-C bond content in MG may be attributed to the presence of GA. In the O 1s spectrum, the characteristic peak Ti-C-(OH)$_x$ of MG shifted from 532 eV in MXene to a higher binding energy of 532.5 eV, with a notable increase in intensity.[7] These findings indicate the formation of more robust hydrogen bond interactions in MG, consistent with the results obtained from FTIR spectroscopy. It is noteworthy that the MX-O peak exhibited the characteristic TiO$_2$ peak at 529.9 eV, whereas the MG-O peak appeared predominantly as Ti-C-(OH)$_x$ at 532.5 eV, suggesting the antioxidant properties of MG. Also, according to the integral area, the content of Ti^{4+} in MX-O accounted for 40.39%, while that in MG-O was only 10.49%.
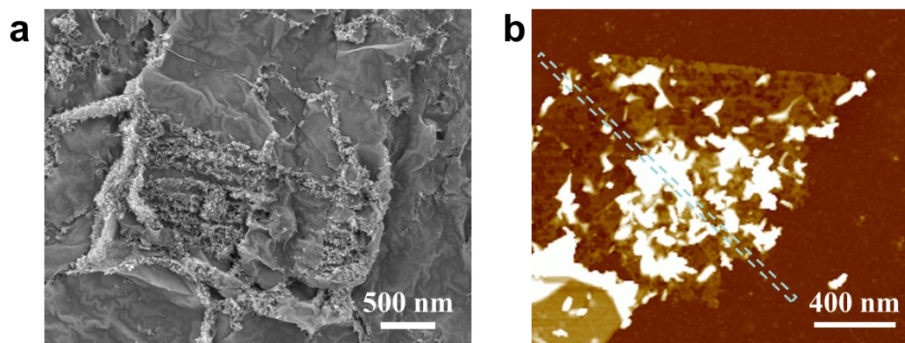
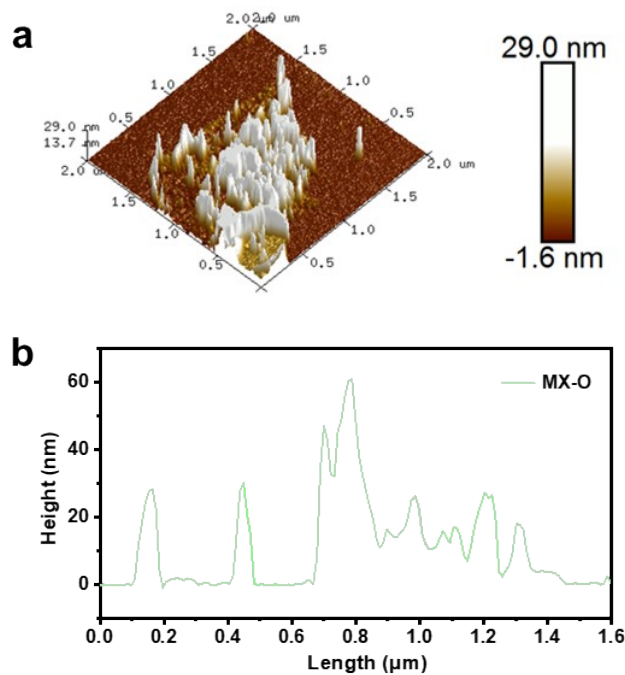**Figure S9.** (a) SEM and (b) AFM image of MXene nanosheet after oxidation.

Figure S10. (a) 3D AFM image of MXene nanosheet after oxidation. (b) Height curves of MXene nanosheet after oxidation (MX-O) obtained from (Figure S9b). The oxidation of MXene begins at the periphery and progresses inward. As the oxidation process intensifies, "branches" form at the edges of the MXene lamella, and nanoparticles emerge on the lamella's surface (Figure S9). During the aging process, these branches extend from the edges toward the basal plane, a phenomenon consistent with the "scissors effect," which leads to significant morphological differences between oxidized MXene and its reduced form, MG.[8] Additionally, AFM images provide further evidence of these distinct morphological variations, illustrating that MG exhibits a regular structure characterized by a pronounced edge and a lower interior, whereas oxidized MXene (MX-O) displays uneven height profiles (Figure S10).
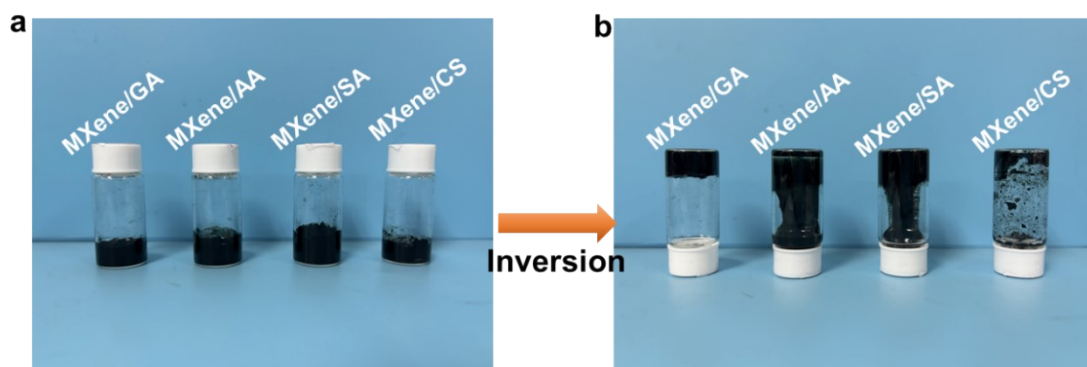
Figure S11. Diagram of various MXene/GA, MXene/AA, MXene/SA, MXene/CS inks with the same additive content in bottles (a) and in inverted bottles (b). MXene composite solutions of several common hydrogel antioxidants (short-chain sodium alginate (SA), chitosan (CS), or ascorbic acid (AA)) were prepared. As illustrated in Figure S8a, 0.02g of the additive was dissolved in 2ml of MXene solution. Subsequently, in Figure S8b, it is evident that MXene/GA maintains a gel-like state when the bottle is inverted, while MXene/AA or MXene/SA exhibit flow, and MXene/CS undergoes flocculation instead of forming a homogeneous solution suitable for ink applications. Notably, at equivalent additive concentrations, MXene/GA retains its gel-like consistency and can be easily converted to a liquid state with a simple manual agitation.
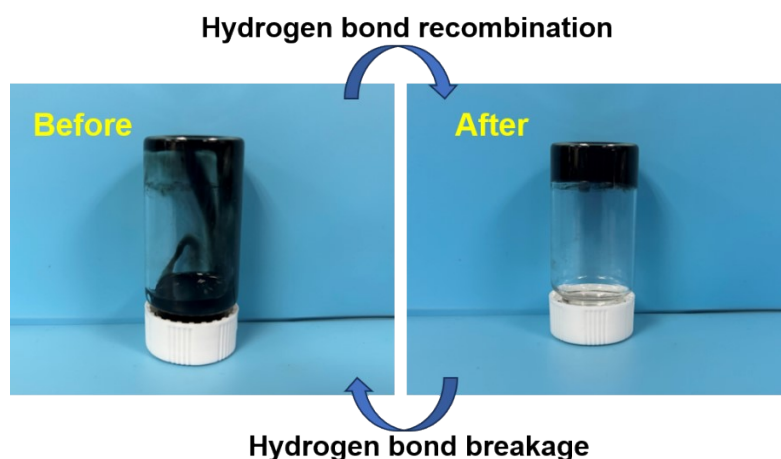
Figure S12. MG$_1$ inks perform hydrogen bond reconstruction at minimum 65 °C.
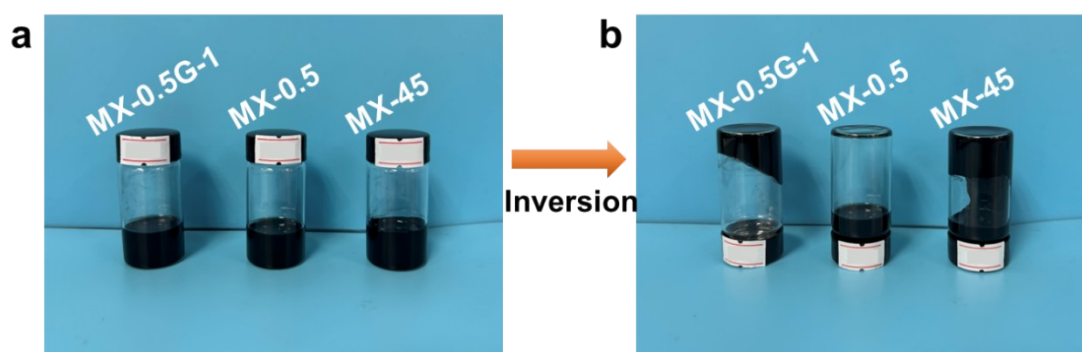

Figure S13. Diagram of MX-0.5G-1, MX-0.5, MX-45 inks in bottles (a) and in inverted bottles (b). Illustrated in Figure S10a, samples were prepared in the sample bottle with low-concentration (0.5 mg/ml) MXene ink, low-concentration (0.5 mg/ml) MG ink with tiny GA additive (1 wt%), high-concentration (45 mg/ml) MXene ink, for comparative analysis. Specifically, MXene at very low concentrations (0.5 mg/ml) is denoted as MX-0.5, 1wt% of GA is labeled as G-1, and high concentrations of MXene (45mg/ml) are designated as MX-45. When the bottle is inverted, both low and high concentration MXene solutions flow, while MG remains solidified (Figure S10b). In supplementary videos 1, it is observed that MX-0.5 flows rapidly on an inclined glass plate, whereas MX-0.5G-1 exhibits a slow flow state, even slower than MX-45.
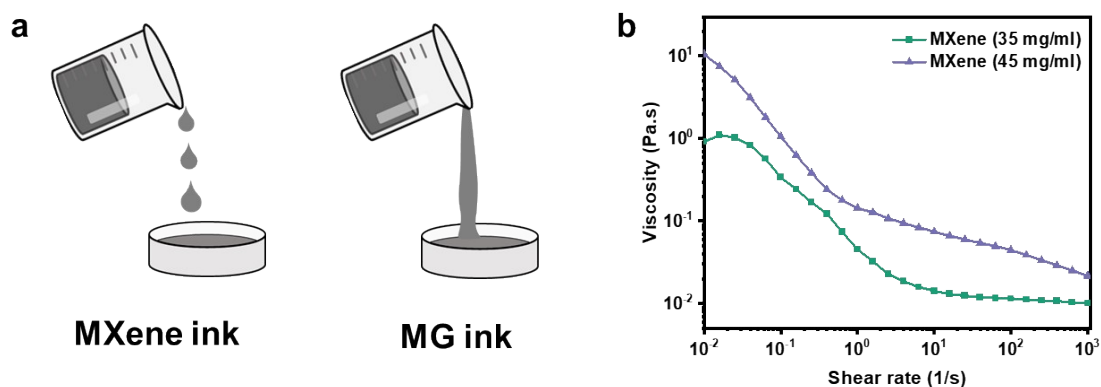
Figure S14. (a) Illustration of MXene and MG ink drips. (b) The viscosity versus shear rate curves for high-concentration MXene inks with content of 35 mg/ml and 45 mg/ml, respectively. Figure S11 further demonstrate that when the MXene concentration is very low, the addition of a small amount of GA can achieve viscosity levels equal to or greater than high-concentration MXene.
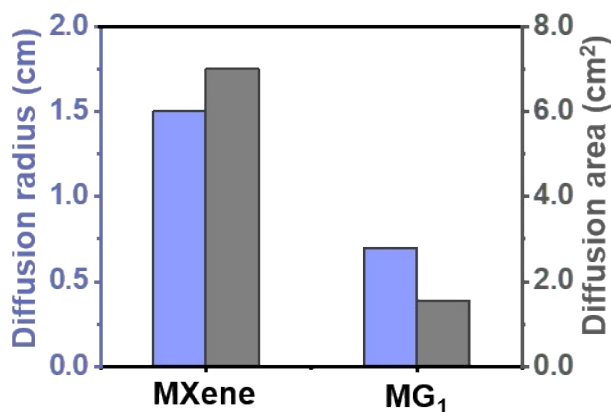

Figure S15. Diffusion radius and area of MXene and MG_1 on nylon paper.
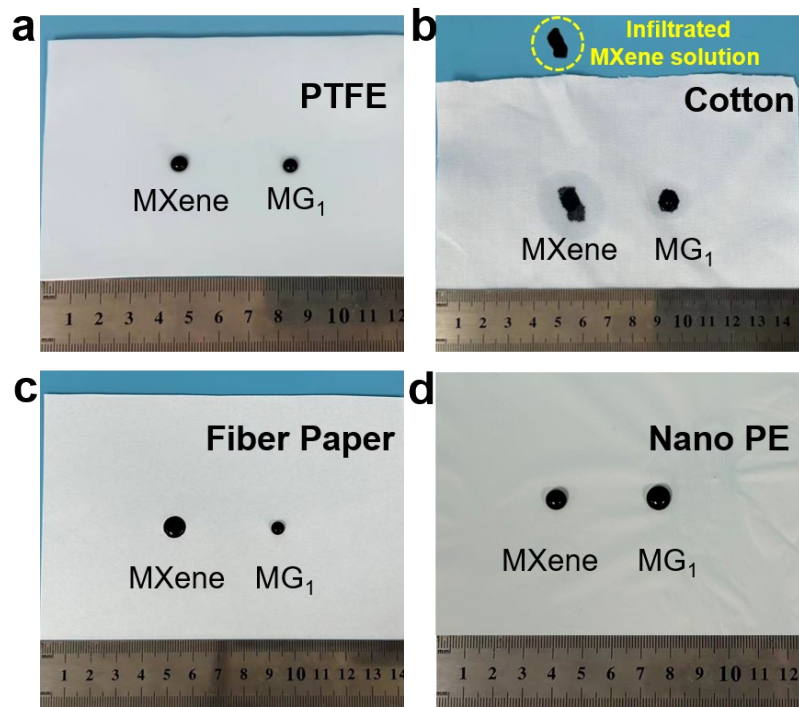
Figure S16. Digital image showing diffusion capacity of MXene and MG$_1$ inks on different substrates viewed from a vertical angle.
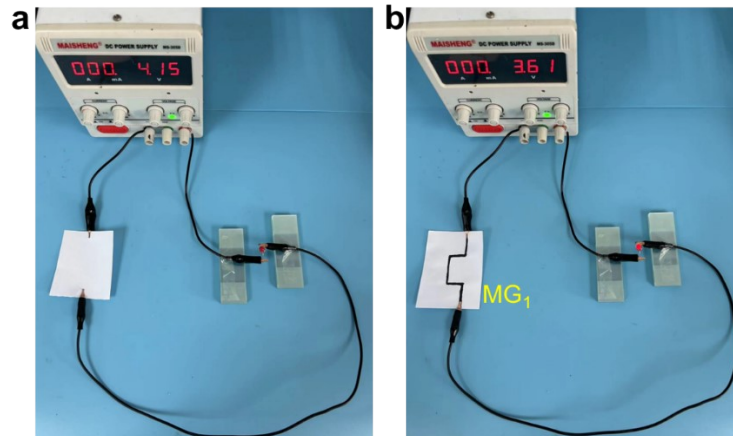

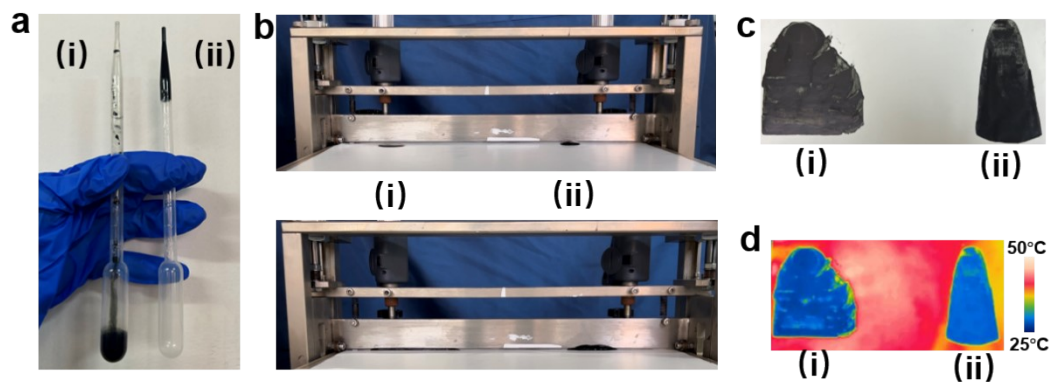**Figure S17**. Electrical conductivity of MG$_1$ ink on an A4 paper.

Figure S18. Blade coating of (i) MXene and (ii) MG₁ ink on nylon substrate with MXene solution of 15 mg/ml. Figure S15a depicts MXene (i) and MG (ii) positioned in an inverted manner within a dropper, where the gelation network prevents backflow of MG. Figure S15b showcases the simultaneous process of MXene and MG, highlighting the superior shape retention of MG ink, resulting in a more uniform blade-coated pattern. Figure S15c, S15d further elucidates this uniformity using digital and infrared cameras.
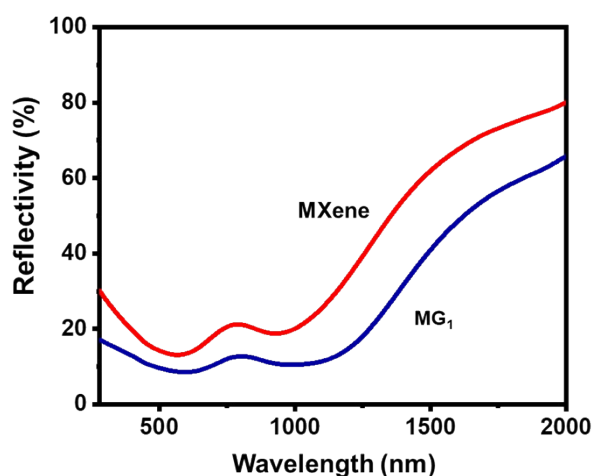

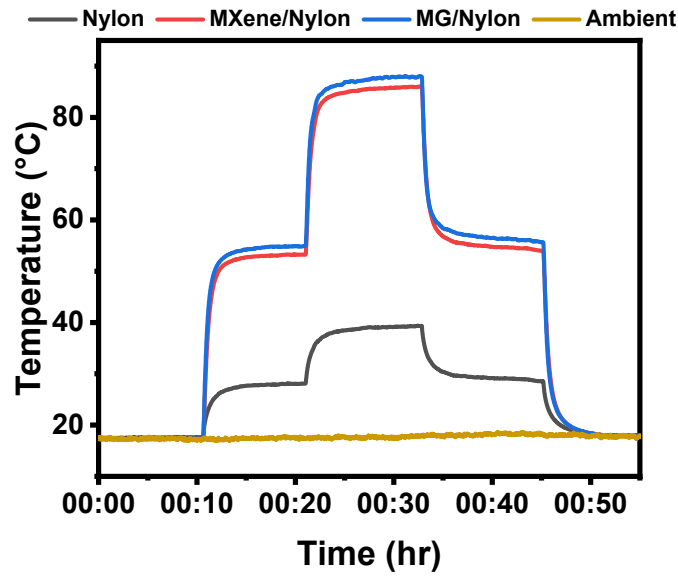**Figure S19**. Reflectivity of MXene and MG₁ in UV-vis-NIR spectrum.

Figure S20. Temperature versus solar irradiation of MXene/Nylon, MG/Nylon, and Nylon films simulated by a xenon lamp.

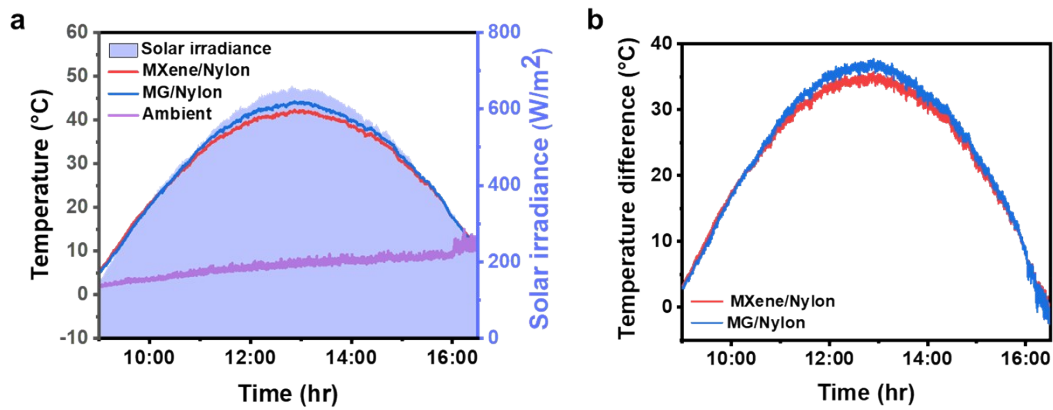**Figure S21.** (a) Real-time monitored temperature curves of MXene/Nylon and MG/Nylon (January 27, 2024). (b) Real-time temperature difference between MXene/Nylon or MG/Nylon and ambient for outdoor solar irradiation conversion.
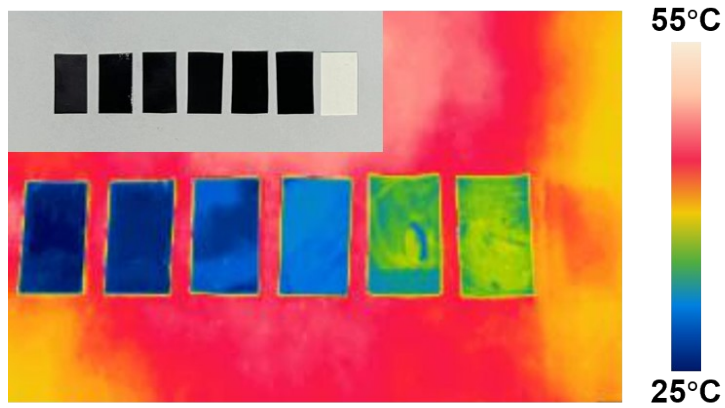
Figure S22. IR thermogram of different MG inks coated on nylon paper.
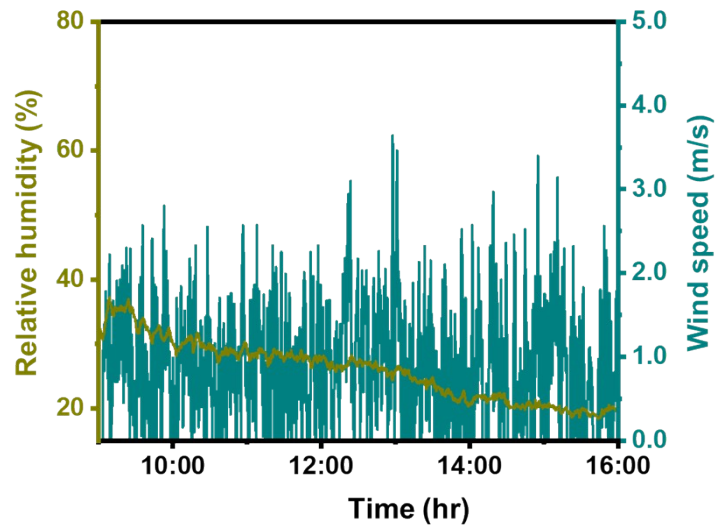
Figure S23. Real-time monitored wind speed and relative humidity for outdoor solar

irradiation conversion (June 14, 2023).
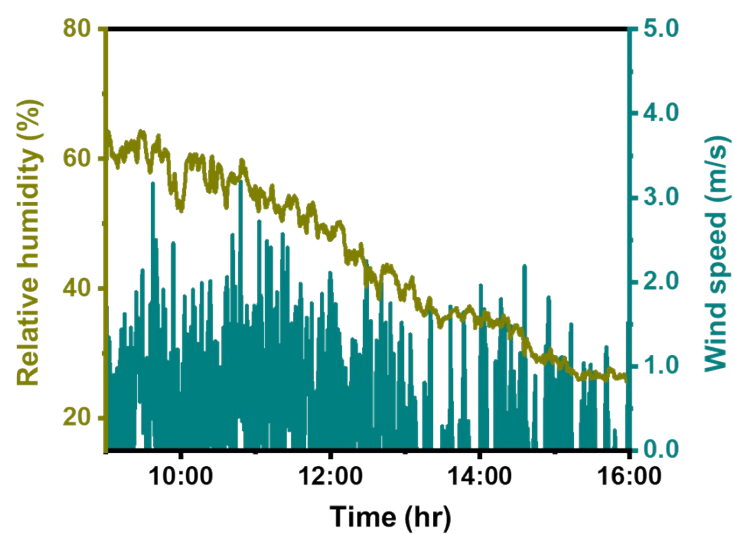
Figure S24. Real-time monitored wind speed and relative humidity for aging experiments (July 22, 2023).
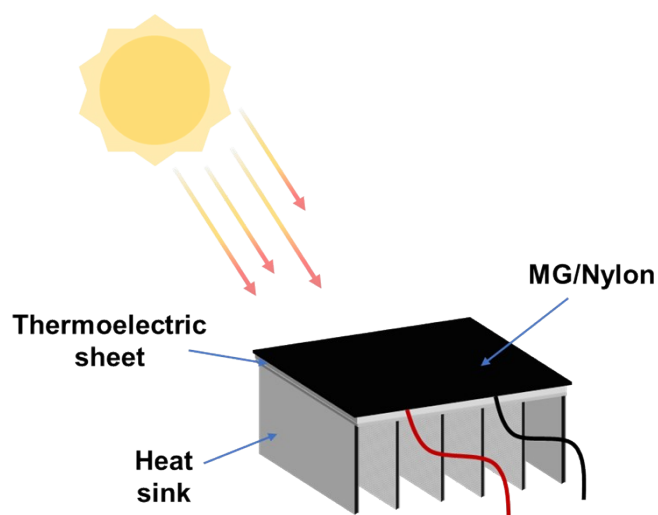
Figure S25. Schematic of solar thermal-electricity conversion device. The upper surface of the commercial thermoelectric conversion sheet affixed with MG/nylon is sealed with foam and PE plastic wrap, and the lower surface is exposed to air.
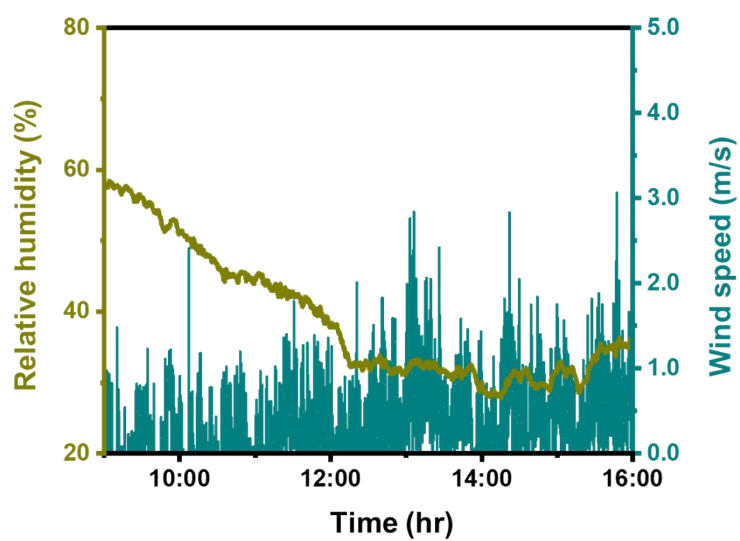
Figure S26. Real-time monitored wind speed and relative humidity for solar thermal-electricity conversion experiments (November 1, 2023).

Table S1. Comparison of long-term oxidation resistance of MXene in reported literatures.

MXene concentration (mg/ml)	Additives	Storage time	Reference
15	Polyanionic salts	21 days	4
6.06	Sodium L-ascorbate	21 days	9
/	Ionic liquid	30 days	10
/	APTES	21 days	11
8.8	Antioxidants	14 days	12
15	PDA	1 month	13
3	Tartaric acid	7 days	14
10	GA	2 months	*This work*

Notes: APTES is (3-Aminopropyl) triethoxysilane; PDA is polydopamine; GA is Glycyrrhizic Acid.

Table S2. Comparison of viscosity, processing method for high-concentration MXene inks in literautres and low-concentration MXene inks in this work. Compared with the processing method of high concentration.

MXene Concentration (mg/ml)	Additive	Viscosity (Pa.s)	Writing	Spray coating	Screen printing	Blade coating	3D printing	Ref.
150	C12E9	/					√	15
80	BEPI	19489			√		√	16
60	PDA	12930	√		√			13
20	NE	1240					√	17
20	dopamine	2419.9				√		18
15	Mg^{2+}-CMC	11000	√			√		19
0.5	**GA**	**31283**	√	√	√	√	√	**This work**

Notes: Viscosity is at shear rate of $0.01\ s^{-1}$; C12E9 is nonaethylene glycol monododecyl ether; BEPI is branched polyethyleneimine; PDA is polydopamine; NE is norepinephrine; CMC is sodium carboxymethyl cellulose; GA is Glycyrrhizic Acid.

References:

1. T. Echániz, I. Setién-Fernández, R. B. Pérez-Sáez, C. Prieto, R. E. Galindo and M. J. Tello, *Sol. Energy Mater. Sol. Cells*, 2015, **140**, 249-252.

2. L. Zhang, H. Y. Zhang, X. T. Yu, L. Q. Xu, D. Wang, X. Y. Lu and A. M. Zhang, *ACS Appl. Mater. Interfaces*, 2022, **14**, 53298-53313.

3. S. Jose, A. Prakash, S. Laha, S. Natarajan and M. L. Reddy, *Dyes Pigment.*, 2014, **107**, 118-126.

4. V. Natu, J. L. Hart, M. Sokol, H. Chiang, M. L. Taheri and M. W. Barsoum, *Angew. Chem.-Int. Edit.*, 2019, **58**, 12655-12660.

5. V. Natu, M. Sokol, L. Verger and M. W. Barsoum, *J. Phys. Chem. C*, 2018, **122**, 27745-27753.

6. S. H. Huang, V. Natu, J. Y. Tao, Y. M. Xia, V. N. Mochalin and M. W. Barsoum, *J. Mater. Chem. A*, 2022, **10**, 22016-22024.

7. Z. Hao, S. Zhang, S. Yang, X. Li, Y. Gao, J. Peng, L. Li, L. Bao and X. Li, *ACS Appl. Energ. Mater*, 2022, **5**, 2898-2908.

8. C. F. J. Zhang, S. Pinilla, N. McEyoy, C. P. Cullen, B. Anasori, E. Long, S. H. Park, A. Seral-Ascaso, A. Shmeliov, D. Krishnan, C. Morant, X. H. Liu, G. S. Duesberg, Y. Gogotsi and V. Nicolosi, *Chem. Mat.*, 2017, **29**, 4848-4856.

9. X. Zhao, A. Vashisth, E. Prehn, W. Sun, S. Shah, T. Habib, Y.X. Chen, Z.Y. Tan, J. Lutkenhaus, M. Radovic and M.J. Green, *Matter*, 2019, **1**, 513-526.

10. H. R. Zhao, J. H. Ding, M. Zhou and H. B. Yu, *ACS Appl. Nano Mater.*, 2021, **4**, 3075-3086.

11. J. J. Ji, L. F. Zhao, Y. F. Shen, S. Q. Liu and Y. J. Zhang, *FlatChem*, 2019, **17**, 100128.

12. X. F. Zhao, H. X. Cao, B. J. Coleman, Z. Y. Tan, I. J. Echols, E. B. Pentzer, J. L. Lutkenhaus, M. Radovic and M. J. Green, *Adv. Mater. Interfaces*, 2022, **9**, 2200480.

13. Z. M. Deng, L. L. Li, P. P. Tang, C. Y. Jiao, Z. Z. Yu, C. M. Koo and H. B. Zhang, *ACS Nano*, 2022, **16**, 16976-16986.

14. M. Zhang, F. Héraly, M. Yi and J. Y. Yuan, *Cell Rep. Phys. Sci.*, 2021, **2**, 100449.

15. G. Shi, Y. X. Zhu, M. Batmunkh, M. Ingram, Y. F. Huang, Z. H. Chen, Y. J. Wei, L. X. Zhong, X. W. Peng and Y. L. Zhong, *ACS Nano*, 2022, **16**, 14723-14736.

16. S. R. Liu, Q. Meng, Y. D. Gao, J. Z. Zhang, J. R. Li, Y. W. Yang, X. M. Zhang, H. P. Li and X. Y. Liu, *J. Mater. Chem. A*, 2023, **11**, 13238-13248.

17. P. Z. Jiang, Z. M. Deng, P. Min, L. X. Ye, C. Z. Qi, H. Y. Zhao, J. Liu, H. B. Zhang and Z. Z. Yu, *Nano Res.*, 2024, **17**, 1585-1594.

18. Z. M. Deng, P. Z. Jiang, Z. G. Wang, L. Xu, Z. Z. Yu and H. B. Zhang, *Small*, 2023, **19**, 2304278.

19. D. R. Chen, Y. Long, Z. T. Wu, X. M. Dong, N. Wang, J. Y. Yu, D. L. Han, Y. Tao and Q. H. Yang, *Adv. Funct. Mater.*, 2022, **32**, 2204372.